International Journal of Naval Architecture and Ocean Engineering 13 (2021) 86–101

Contents lists available at ScienceDirect

International Journal of Naval Architecture and Ocean Engineering

journal homepage: http://www.journals.elsevier.com/international-journal-of-naval-architecture-and-ocean-engineering/

The effects of geometrical buoy shape with nonlinear Froude-Krylov force on a heaving buoy point absorber

Sung-Jae Kim [a, b], Weoncheol Koo [a, *], Moo-Hyun Kim [b]

[a] Department of Naval Architecture and Ocean Engineering, Inha University, Incheon, Republic of Korea
[b] Department of Ocean Engineering, Texas A&M University, College Station, TX, USA

ARTICLE INFO

Article history:
Received 4 August 2020
Received in revised form
3 December 2020
Accepted 27 January 2021
Available online 27 February 2021

Keywords:
Nonlinear Froude-Krylov force
Buoy shape
Wave energy converter
Response amplitude operator
Hydraulic power take-off system
Latching control strategy

ABSTRACT

This study examined the effects of buoy shape and Nonlinear Froude-Krylov force (NFK) on a heaving-buoy-type Wave Energy Converter (WEC). Based on the Maclaurin expansion, the theoretical solutions of the NFK were derived for three different buoy shapes; hemispheric buoy, circular vertical cylinder, and truncated conical cylinder. A hydraulic power take-off system was adopted, and the latching control strategy was applied to maximize the extracted power from the WEC. The nonlinear effects of the Froude-Krylov force and restoring force on the heaving point absorber were investigated by comparing the heave Response Amplitude Operator (RAO) and time-averaged power extraction. The results showed that the conventional linear analyses were overestimated by up to 50% under the high amplitude wave condition. The latching control strategy was the most effective when peak wave period of regular or irregular wave was 0.4–0.45 times the heave natural period of the buoy.

1. Introduction

The Wave Energy Converter (WEC) can be classified as moveable-body type, oscillating-water-column type, and over-topping/overflow type according to their energy-conversion methodology. Among these, the movable-body-type WEC generates powers by converting wave energy to WEC's kinetic energy. WECs can also be classified according to buoy's mode of motion, such as heaving buoy type, pendulum type, oscillating surge-type (Oyster type) and so on. The heaving-buoy-type WEC can be extended easily to a renewable energy farm or a hybrid renewable energy system. The heaving-buoy-type WEC has very large motion around its natural frequency because of the resonance phenomenon, but the resonance region is often narrow-banded. Therefore, a control technique is required to increase energy extraction (Folley et al., 2015). To apply the control technique, the interaction between the floating body and power take-off (PTO) as well as the range of nonlinear factors due to the application of the control method, should be considered (Nazari et al., 2013; Kalofotias, 2016).

Since 2000, numerous studies have been carried out to estimate the nonlinear hydrodynamic effects of heaving-buoy-type WECs. Weakly nonlinear analysis or fully nonlinear analysis was performed to consider the nonlinearity of floating body motion. The weakly nonlinear analysis often considered the Nonlinear Froude-Krylov force (NFK) in addition to the first-order (linear) hydrodynamic analysis based on the radiation/diffraction problem. In some cases, the second-order diffraction force was also adopted. The nonlinear Froude-Krylov force, which is the force from undisturbed incident waves, can be obtained by integrating the pressure over the instantaneous wetted buoy surface. The method of calculating the NFK may include a remeshing scheme or a theoretical solution. The remeshing numerical scheme generates the instantaneous wetted-surface meshes according to the buoy motion and wave elevation around the body (Jang and Kim, 2020). Babarit et al. (2009) and Merigaud et al. (2012) applied the remeshing scheme to evaluate the nonlinear Froude-Krylov force and the double-frequency diffraction force on a WEC buoy, respectively. Giorgi and Ringwood (2017) derived a theoretical solution of the Froude-Krylov force for an axisymmetric heaving buoy using the Maclaurin expansion method under regular wave conditions. They described the wetted body surface theoretically based on the cylindrical coordinate system. They then simplified the instantaneous water line around the body based on the long wave assumption and adopted a simple PTO modeling as a linear damper. They

* Corresponding author.
E-mail address: wckoo@inha.ac.kr (W. Koo).
Peer review under responsibility of The Society of Naval Architects of Korea.

https://doi.org/10.1016/j.ijnaoe.2021.01.008

considered nine types of different numerical approaches, including Computational Fluid Dynamics (CFD). They reported that the nonlinear Froude-Krylov forces, nonlinear restoring forces, and nonlinear viscous forces are very important in applying the control strategies. Giorgi and Ringwood (2018) derived a theoretical solution of the nonlinear Froude-Krylov force for a three-degree-of-freedom point absorber under regular wave conditions. They showed that the calculation time using the theoretical solution was shorter than that using the remeshing technique. Kim et al. (2019b) considered the nonlinear Froude-Krylov force and hydraulic PTO system under regular wave conditions. Parametric studies on the hydraulic PTO condition of a hemispherical heaving-buoy WEC were carried out. The capture width of the WEC decreased in the longwave region as the wave amplitude increased.

This study derived the theoretical solutions of nonlinear Froude-Krylov forces on three different geometries of WEC buoys (a hemispherical buoy, a vertical circular cylindrical buoy, and a truncated conical buoy) based on Giorgi and Ringwood (2017). The theoretical solution of the nonlinear Froude-Krylov force was verified by comparison with the results of the remeshing technique. Based on them, the hydraulic PTO system and latching control strategy were applied to estimate WEC's hydrodynamic and power take-off performances. The effects of the nonlinear Froude-Krylov force were identified, and the relationship between the incident wave period (or amplitude) and latching control strategy under regular wave conditions was investigated. Finally, based on the results of regular wave analysis, the effects of the nonlinear Froude-Krylov force on WEC buoys with latching control under irregular wave conditions were estimated, which can be regarded as an extension of the previously developed latching control strategy for regular waves.

2. Mathematical formulation

2.1. Equation of motion for a rigid body

All forces acting on a heaving body type WEC can be expressed as

$$m\ddot{\xi} = F_D + F_R + F_{FK} + F_{static} + F_{vis} + F_{PTO} - W \tag{1}$$

where m and $\ddot{\xi}$ are the mass of a buoy and acceleration of vertical motion, respectively. F_D, F_R, F_{FK}, F_{static}, F_{vis}, F_{PTO}, and W denote the diffraction force, radiation force, Froude-Krylov force, hydrostatic force, viscous damping force, PTO force, and gravity force, respectively. Among these force components, the radiation force and diffraction force can be obtained by solving the radiation problem and diffraction problem, respectively. The radiation force can be decomposed into two terms: one that is proportional to the acceleration and the other that is proportional to the velocity of a buoy. This force also satisfies the linearity of functions and the Bound Input and Bound Output stability (BIBO), so it can be expressed using the convolution terms.

$$F_R(\omega) = -M_a(\omega)\ddot{\xi}(\omega) - b(\omega)\dot{\xi}(\omega) \tag{2}$$

$$F_R(t) = -M_a(\infty)\ddot{\xi}(t) - \int_0^t K(t-\tau)\dot{\xi}(\tau)d\tau \tag{3}$$

where M_a and b are the added mass and radiation damping coefficient. $K(t)$ is the memory function or impulse response function expressed as Eq. (4).

$$\begin{aligned} K(t) &= -\frac{2}{\pi}\int_0^\infty b(\omega)\cos(\omega t)d\omega \\ &= -\frac{2}{\pi}\int_0^\infty (M_a(\omega) - M_a(\infty))\omega\sin(\omega t)d\omega \end{aligned} \tag{4}$$

The frequency-dependent diffraction force can be expressed as Eq. (5).

$$F_D(\omega) = -\rho\int_{S_B}\frac{\partial\phi_D}{\partial t}n_z dS \tag{5}$$

$$F_D(t) = \sum_{i=1}^{n_w} A_i\left|F_{D\_i}(\omega)\right|\cos(\omega_i t + \theta_i + \theta_{r\_i}) \tag{6}$$

where ρ, ϕ_D, and $n_z$is the water density, diffraction velocity potential, and z-directional component of the normal vector, respectively. A_i, F_{D_i}, ω_i, θ_i, and θ_{r_i} are the incident wave amplitude, diffraction force in the frequency domain, wave frequency, phase angle of the diffraction force, and random phase angle of the ith wave, respectively. n_w is the number of incident wave components. Under regular single wave conditions, only one frequency component was applied, and the random phase angle was set to zero. Under irregular wave conditions, the amplitude of the i-th wave can be obtained (Eq. (7)) using the PM spectrum (Eq. (8)).

$$A_i = \sqrt{2S_w(\omega_i)d\omega} \tag{7}$$

$$S_w(\omega) = \frac{173H_s^2}{T_1^4\omega^5}\exp\left(\frac{-692}{T_1^4\omega^4}\right) \tag{8}$$

where S_w, H_s, and T_1 are PM wave spectrum, significant wave height, and mean centroid wave period, respectively. The commercial hydrodynamic analysis software WAMIT (WAMIT, 2019) was used to calculate the hydrodynamic coefficients (added mass, radiation damping coefficient, and diffraction force). The program is based on the wave green function and boundary element method.

2.2. Froude-Krylov force

The Froude-Krylov force is the force acting on the body from an undisturbed incident wave. This force can be obtained using the incident wave velocity potential, as shown in Eq. (9) and Eq. (10).

$$p(\vec{x}, t) = -\rho\frac{\partial\phi_I}{\partial t} = -\rho g A e^{kz}\cos(kx\cos\beta + ky\sin\beta - \omega t) \tag{9}$$

$$\begin{aligned} F_{FK} = \int_{S_B} p(\vec{x}, t)n_z dS = \int_{S_B}\Big(&-\rho g A e^{kz}\cos(kx\cos\beta + ky\sin\beta \\ &- \omega t)\Big)n_z dS \end{aligned} \tag{10}$$

where $\vec{x}$ is the position of a collocation point (x, y, z) on the boundary element. ϕ_I, g, k, β, and S_B are the incident wave velocity potential, gravitational acceleration, wave number, angle of the incident wave, and body surface, respectively. To express the theoretical solution of nonlinear Froude-Krylov force on an axisymmetric body, the coordinate system should be transferred from the Cartesian coordinate to the cylindrical coordinate (Giorgi

and Ringwood, 2017). In this scheme, the equation of the body radius along the z-axis was derived according to the shape of the heaving buoy. The nonlinear Froude-Krylov force is obtained by integrating the incident-wave pressure over the instantaneous wetted body surface that changes according to the body motions and incident wave elevations at every time step. In addition, the water particle velocity and hydrodynamic pressure above the mean water level are expressed by vertical stretching.

2.2.1. Theoretical solution of the Froude-Krylov force for a hemispherical buoy

Giorgi and Ringwood (2017) transformed the Cartesian co-ordinates, (x,y,z), into the cylindrical coordinates system (r,θ,σ) to derive the theoretical solution of Froude-Krylov force acting on a hemispherical buoy as Fig. 1(a). The equation of a radius along the z-axis on a hemisphere can be described using Eq. (11).

$$r = f(\sigma) = \sqrt{R^2 - (\sigma - \xi)^2} \tag{11}$$

where R and ξ are the radius and vertical displacement of the hemispherical buoy, respectively. The vertical Froude-Krylov force can be obtained as Eq. (12).

$$F_{FK} = \int_0^{2\pi}\int_{\sigma_2}^{\sigma_1} \rho g A e^{kz} \cos(kf(\sigma)\cos\theta - \omega t) f'(\sigma) f(\sigma) d\sigma d\theta \tag{12}$$

In this study, the lower shape of the WEC floating buoy was different, but the upper shape of all floating buoys was fixed in the form of vertical circular cylinders. Therefore, the effective range of the z-axis is expressed as Eq. (13).

$$\begin{cases} \sigma_1 = \min(\eta(t), \xi) \\ \sigma_2 = \xi - d \end{cases} \tag{13}$$

where η and d are wave elevation at the center point of a buoy and draft of a buoy, respectively. Eq. (12) can be converted to Eq. (14), which can be integrated directly using the Maclaurin expansion method to obtain the Froude-Krylov force.2

$$\begin{aligned} F_{FK} &= \rho g A \cos\omega t \int_0^{2\pi}\int_{\sigma_2}^{\sigma_1} e^{kz} C_{sphere}(\sigma,\theta)(\sigma-\xi) d\sigma d\theta \\ C_{sphere}(\sigma,\theta) &= 1 - \frac{\left(k\sqrt{R^2-(\sigma-\xi)^2}\cos\theta\right)^2}{2!} + \frac{\left(k\sqrt{R^2-(\sigma-\xi)^2}\cos\theta\right)^4}{4!} - \frac{\left(k\sqrt{R^2-(\sigma-\xi)^2}\cos\theta\right)^6}{6!} + \cdots \end{aligned} \tag{14}$$

2.2.2. Theoretical solution of the Froude-Krylov force for a vertical cylindrical buoy

For a circular cylinder, the bottom surface of the buoy is only affected by the incident wave for the vertical Froude-Krylov force. Therefore, the coordinate system of the bottom can be expressed as Eq. (15)(see Fig. 1(b)). The product of dS and n_z can be presented as Eq. (16) according to the coordinate transformation.

$$\begin{cases} x(\theta) = r\cos\theta \\ y(\theta) = r\sin\theta \\ z = \sigma_2 \end{cases} \tag{15}$$

$$n_z dS = r dr d\theta \tag{16}$$

Substituting Eqs. (15) and (16) into Eq. (10) and applying the

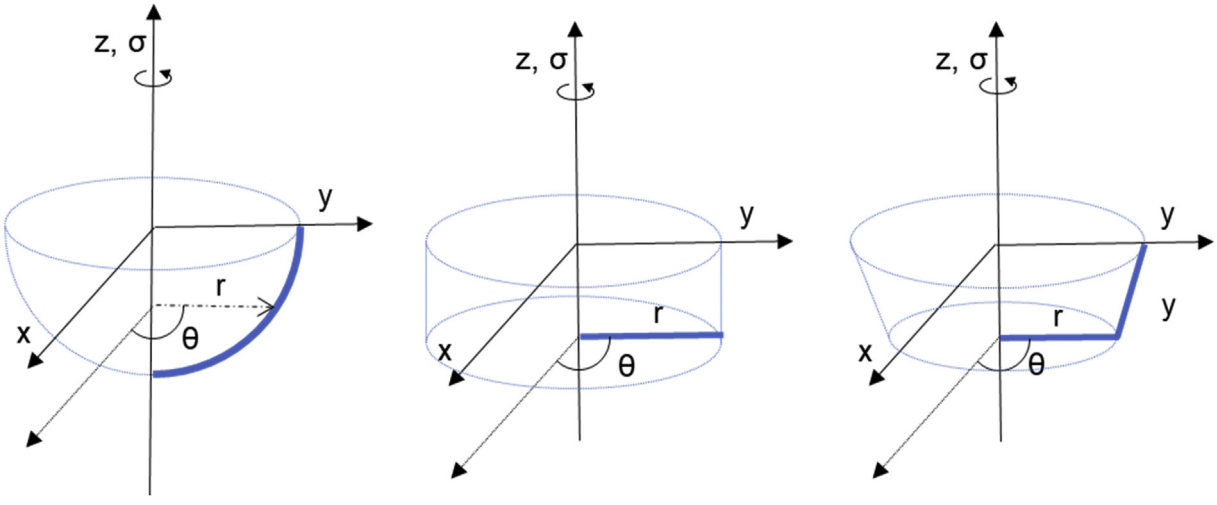

(a) Hemispherical buoy (b) Vertical cylindrical buoy (c) Truncated conical buoy

Fig. 1. Schematic coordinate system of various floating bodies for the Froude-Krylov force.

cosine law and Maclaurin expansion, the theoretical solution of the Froude-Krylov force for a circular vertical cylindrical buoy is finalized as Eq. (17).

$$F_{FK} = r\rho g A e^{k(\xi-d)}\cos(\omega t)\left(R^2\pi - \frac{k^2}{2!}\frac{R^4}{4}\pi + \frac{k^4}{4!}\frac{R^6}{6}\frac{3}{4}\pi - \frac{k^6}{6!}\frac{R^8}{8}\frac{5}{8}\pi + \cdots\right) \tag{17}$$

2.2.3. Theoretical solution of the Froude-Krylov force for a truncated conical buoy

To calculate the Froude-Krylov force for a truncated conical buoy, it should be divided into the lateral and bottom parts of a truncated cone as Fig. 1(c). For the side part, the equation for the radius along the z-axis can be expressed as Eq. (18).

$$f(\sigma) = a(\sigma - \xi) + R \tag{18}$$

where a is the slope of the side part of a truncated cone. Substituting Eq. (18) into Eq. (12) and applying the cosine law and Maclaurin expansion, the Froude-Krylov force of the side part can be obtained as Eq. (19).

$$F_{FK\_slope} = a\rho g A\cos(\omega t)\int_0^{2\pi}\int_{\sigma_2}^{\sigma_1} e^{k\sigma}C_{cone}(\sigma,\theta)d\sigma d\theta$$
$$C_{cone}(\sigma,\theta) = f(\sigma) - \frac{k^2 f(\sigma)^3\cos^2\theta}{2!} + \frac{k^4 f(\sigma)^5\cos^4\theta}{4!} - \frac{k^6 f(\sigma)^7\cos^6\theta}{6!} + \cdots \tag{19}$$

At the same time, using Eq. (17), the Froude-Krylov force of the bottom part of a truncated cone can be expressed as Eq. (20).

$$F_{FK\_bottom} = \rho g A e^{k(\xi-d)}\cos\omega t\left(R\prime^2\pi - \frac{k^2}{2}\frac{R\prime^4}{4}\pi + \frac{k^4}{4!}\frac{R\prime^6}{6}\frac{3}{4}\pi - \frac{k^6}{6!}\frac{R\prime^8}{8}\frac{5}{8}\pi + \cdots\right) \tag{20}$$

where R' is the radius of the bottom of the truncated conical buoy. Finally, the total Froude-Krylov force can be obtained.

$$F_{FK} = F_{FK\_slope} + F_{FK\_bottom} \tag{21}$$

2.3. Hydrostatic force

The static force can be obtained using the hydrostatic pressure acting on the floating body.

$$F_{static} = \int_{S_B}(-\rho g z)n_z dS \tag{22}$$

This can be revised by transforming the coordinate system from the Cartesian coordinate to the cylindrical coordinate system. First, the static force for the hemispherical buoy can be expressed as Eq. (23)

$$F_{static} = -2\pi\rho g\int_{\xi-d}^{\sigma_1}\left(\sigma^2-\sigma\right)d\sigma = -2\pi\rho g\left\{\frac{1}{6}\xi^3 - \frac{1}{2}\left(\sigma_1^2+d^2\right)\xi + \frac{1}{3}\left(\sigma_1^3+d^3\right)\right\} \tag{23}$$

The static force for the cylindrical buoy can be described using Eq. (24)

$$F_{static} = -\rho g A_w(\xi - d) \tag{24}$$

The static force for the truncated conical buoy should be calculated separately for the lateral and bottom parts. For each part, the formula can be expressed using Eqs. (25) and (26). Each static force can be combined and expressed as Eq. (27).

$$F_{static\_slope} = -2\pi a\rho g\left[\frac{1}{6}a\xi^3 - \frac{R}{2}\xi^2 + \left\{Rd - \frac{a}{2}\left(\sigma_1^2+a^2\right)\times\right\} + \left\{\frac{a}{3}\left(\sigma_1^3+d^3\right) + \frac{R}{2}\left(\sigma_1^2-d^2\right)\right\}\right] \tag{25}$$

$$F_{static\_bottom} = -\rho g(\xi - d)R\prime^2\pi \tag{26}$$

Table 1
Geometric specifications of the three different buoys.

Item [unit]	Hemisphere (Model 1)	Circular cylinder (Model 2)	Truncated cone (Model 3)
Radius [m]	2.5	2.5	2.5
Draft [m]	2.5	1.667	2.5
Weight [kg]	16,362	16,362	16,362
Water plane area [m^2]	19.634	19.634	19.634

$$F_{static} = -\pi\rho g\left[\frac{1}{3}a^2\xi^3 - aR\xi^2 + \left\{2adR - a^2\left(\sigma_1^2 + d^2\right) + R\prime^2\right\}\xi + \left\{\frac{2a^2}{3}\left(\sigma_1^3 + d^3\right) + aR\left(\sigma_1^2 - d^2\right) - dR\prime^2\right\}\right] \quad (27)$$

2.4. Viscous damping force

To consider the viscous effect, the drag force of the Morrison equation was adopted. The drag force on the body can be described as Eq. (28).

$$F_{vis} = -\frac{1}{2}\rho C_d A_p(\dot{\xi}(t) - v(t))|\dot{\xi}(t) - v(t)| \quad (28)$$

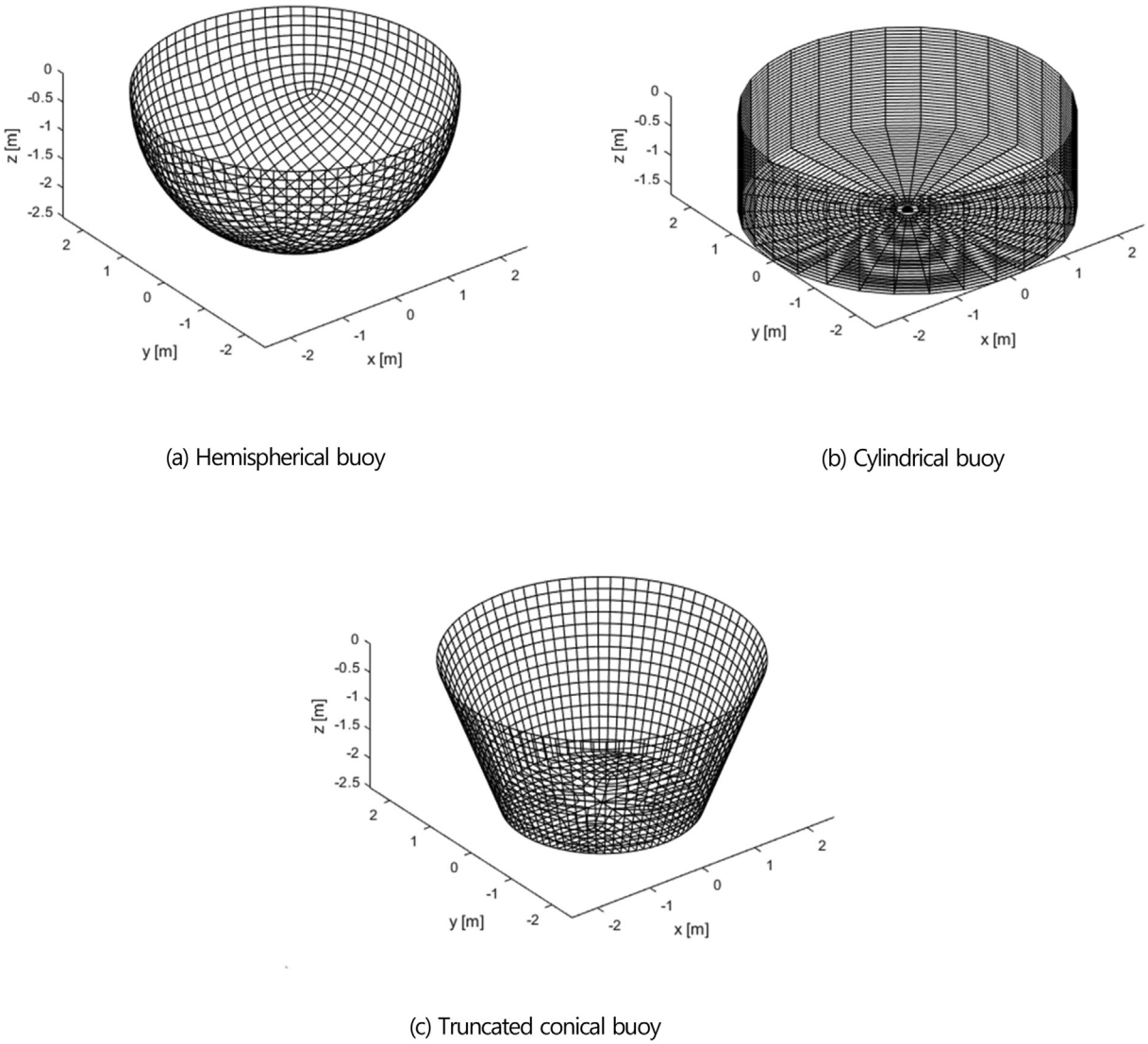

Fig. 2. Numerical models for three different buoys.

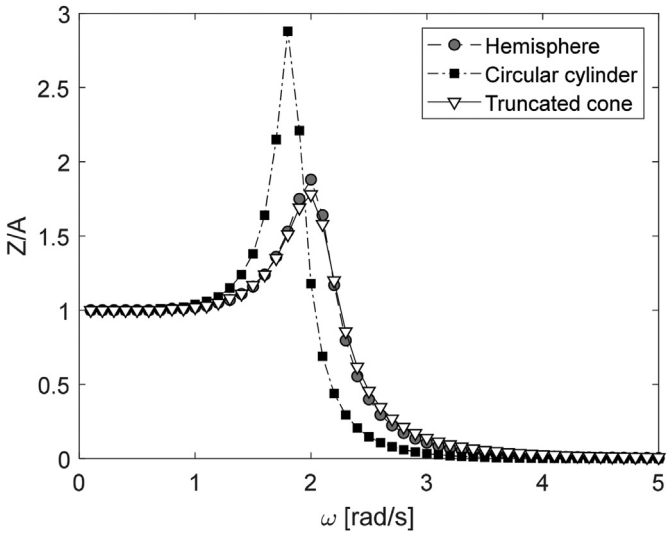

Fig. 3. Comparison of the heave RAOs on various shapes of a buoy.

where C_d, A_p, $\dot{\xi}$, and v are the drag coefficient, projected area, buoy velocity, and water particle velocity, respectively. To represent the viscous damping force accurately, it is very important to estimate the appropriate drag coefficient according to the properties of the floating body. For this, the drag coefficients were estimated primarily from free decay tests or forced oscillation tests. Recently, some studies were conducted to estimate the drag coefficients through CFD analysis. In this study, the drag coefficient of the previous studies was investigated. Based on this, the drag coefficient suitable for this analysis model was selected. Compared to the wave tank experiment, Zurkinden et al. (2014) calculated the drag coefficient of a hemisphere, 0.254 m in diameter, to be 0.2, and Lok et al. (2014) estimated the drag coefficient of a hemisphere, 0.17 m in diameter to 0.175. Giorgi and Ringwood (2017) estimated the drag coefficient of a hemispherical body with a radius of 2.5 m by 0.6 compared to CFD analysis and minimizing the errors. For the drag coefficient of a cylindrical buoy, many studies have been conducted since the 1990s. Gudmestad and Meo (1996) estimated the drag coefficient of cylindrical buoys from 0.65 to 1.05, and Sarpkaya (1986) estimated experimentally that the drag coefficient was between 0.8 and 1.0 for a small Keulegan-Carpenter number. Guo et al. (2018) reported a drag coefficient of 0.93 through experiments. Based on these studies, the drag coefficients of the hemispherical floating body and a cylindrical body were set to 0.6 and 0.95±0.05, respectively, in this study. The drag coefficient of a conical buoy in a few studies was set to 0.8±1.0 (Giorgi et al., 2016).

2.5. PTO force

As a PTO system of a heaving buoy type WEC, a hydraulic system or a linear generator is generally applied. The hydraulic PTO system consists of a hydraulic cylinder that converts vertical buoy motion to fluid flow in a hydraulic circuit, a hydraulic accumulator that protects the hydraulic system or maintains residual pressure, a hydraulic motor and a power generator that produces energy from fluid flow. The hydraulic PTO system can be represented in the form of an approximate coulomb damping force according to its characteristics (Falcao, 2008; Babarit et al., 2012; Kim et al., 2019c).

$$F_{PTO} = -\min(G|\dot{\xi}|, \Delta p S_c)\mathrm{sign}(\dot{\xi}) \tag{29}$$

where Δp and S_c are the pressure difference between High Pressure (HP) and Low Pressure (LP) and the sectional area of a hydraulic cylinder, respectively. G is the slope to reduce the numerical error due to abrupt changes in the PTO force, and as applied by Babarit et al. (2012), applied 100 times the added mass value. The instantaneous extraction power can be obtained by multiplying the PTO force by the velocity of a buoy. Time-averaged extraction power can be expressed as Eq. (30).

$$P_{ex} = \frac{1}{t_e - t_s}\int_{t_s}^{t_e} F_{PTO}\dot{\xi}dt \tag{30}$$

where t_s and t_e are the starting and end times to estimate the time-averaged extraction power, respectively. Under regular wave condition, $t_e - t_s$ was set to be the same as the wave period. A total of 3 h of data was analyzed for irregular wave analysis.

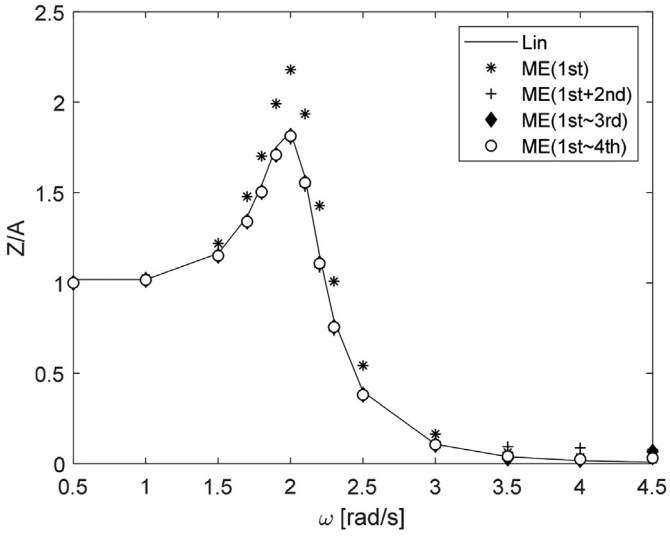

Fig. 4. Comparison of the heave RAOs on the calculation methods of the Froude-Krylov force for a hemispherical buoy (Lin: frequency-domain linear analysis, ME: Maclaurin expansion for NFK force).

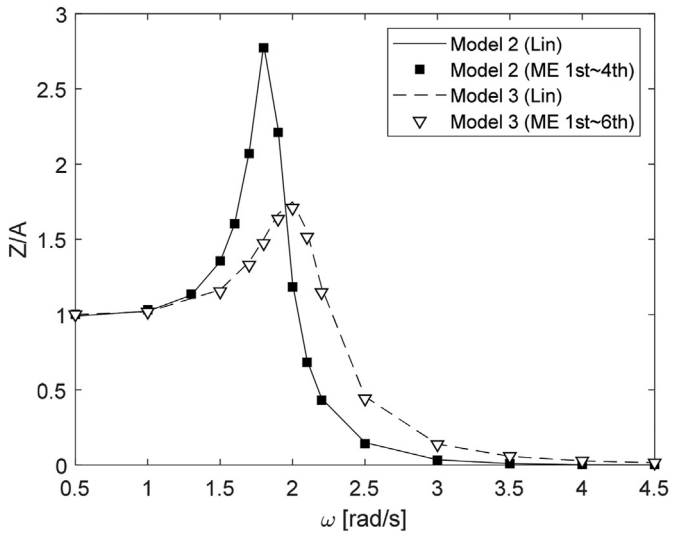

Fig. 5. Comparison of the heave RAOs for various methods of the Froude-Krylov force Model 2 (Cylindrical buoy) and Model 3 (Truncated conical buoy).

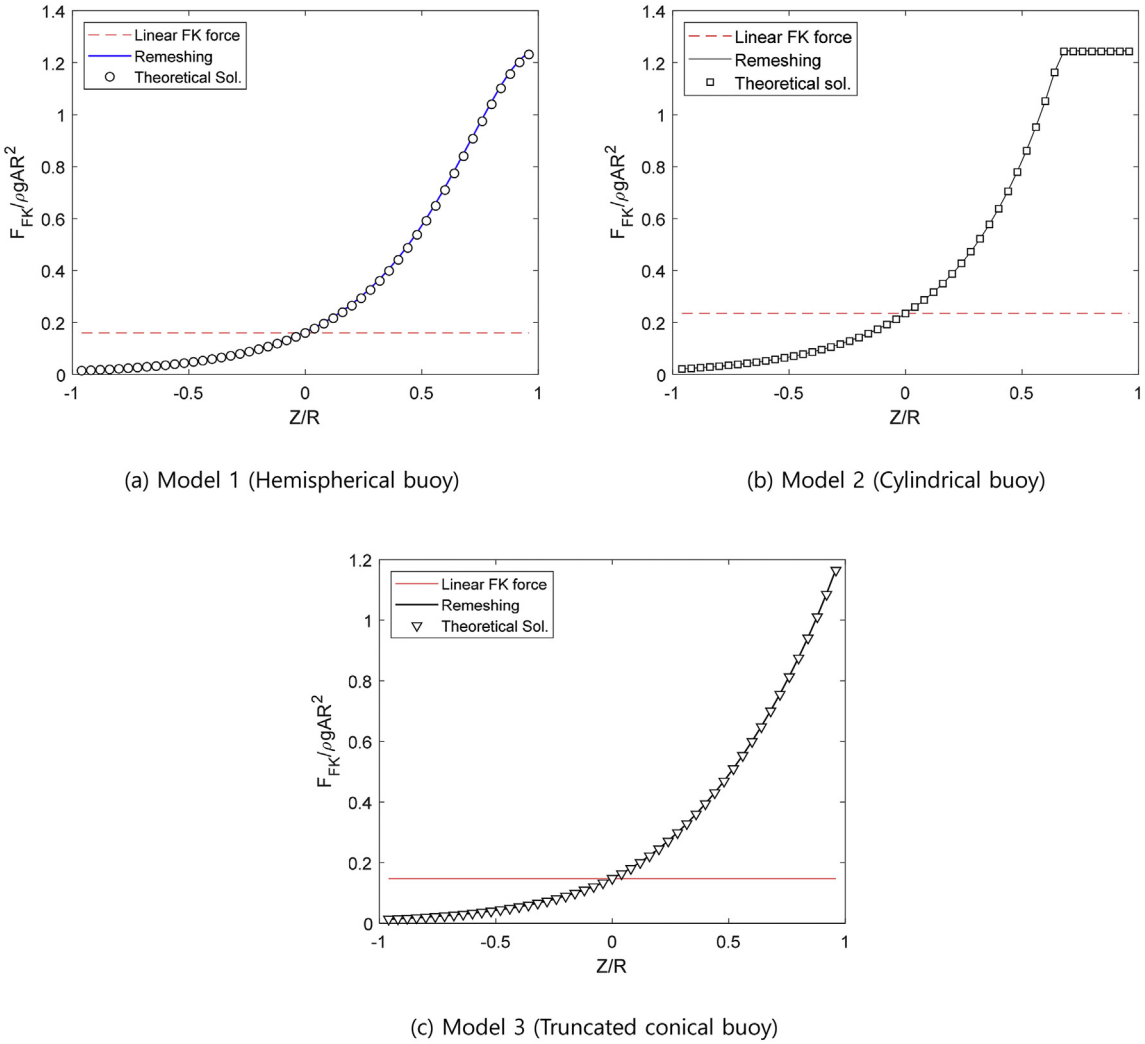

Fig. 6. Comparison of the Froude-Krylov forces on various analysis approaches according to the buoy displacement (a: Hemispherical buoy, b: Circular cylindrical buoy, c: Truncated conical buoy, $\omega = 1$ rad/s).

2.6. Latching control strategy

The latching control is a type of discontinuous phase control technique. This technique controls the phase of buoy displacement by locking and releasing the movement of the buoy for a certain time when the displacement of the buoy reaches its peak due to waves. Because the latching duration is the only variable, the latching control technology is very simple, and its effectiveness has been proven through various researches on control technologies (Hal et al., 2011). The latching duration can be determined using the relationship with the heave natural period of the body (Sheng et al., 2015; Kim et al., 2019a).

$$T_L = \frac{T_c - T_0}{2} \tag{31}$$

where T_L, T_c, and T_0 are the latching duration, characteristic wave period, and the natural period of a buoy, respectively. Under the regular wave condition, the characteristic period is the wave period, and in the irregular wave condition, the characteristic period is the same as the energy period, T_e (Sheng et al., 2015; Cho, 2015). In addition, the motion constraint of the floating body was applied to allow latching control in this study, as expressed in Eq. (32).

$$\begin{cases} \xi(t) = \xi(t_{ls}), & t_{ls} < t < t_{le} \\ \dot{\xi}(t) = 0, & \text{otherwise} \end{cases} \tag{32}$$

where t_{ls} and t_{le} denote the starting time and end time of the latching control, respectively. The effect of the Froude-Krylov force was estimated by applying latching control with the optimal latching duration. The latching control can be applied easily by locking and releasing the valve in the hydraulic circuit for a certain time when the sign of the hydraulic cylinder stroke speed changes.

3. Numerical model and results

In this study, numerical modeling with the same radius, weight, and waterplane area of a hemispherical buoy, cylindrical buoy, and truncated conical buoy was performed. Table 1 lists the specifications of three different floating bodies. The draft of the truncated cone was set to be the same as the draft of the hemispherical buoy and cylindrical cylinder. The weights of all buoys were the same. Fig. 2 shows the numerical model based on Table 1; the number of

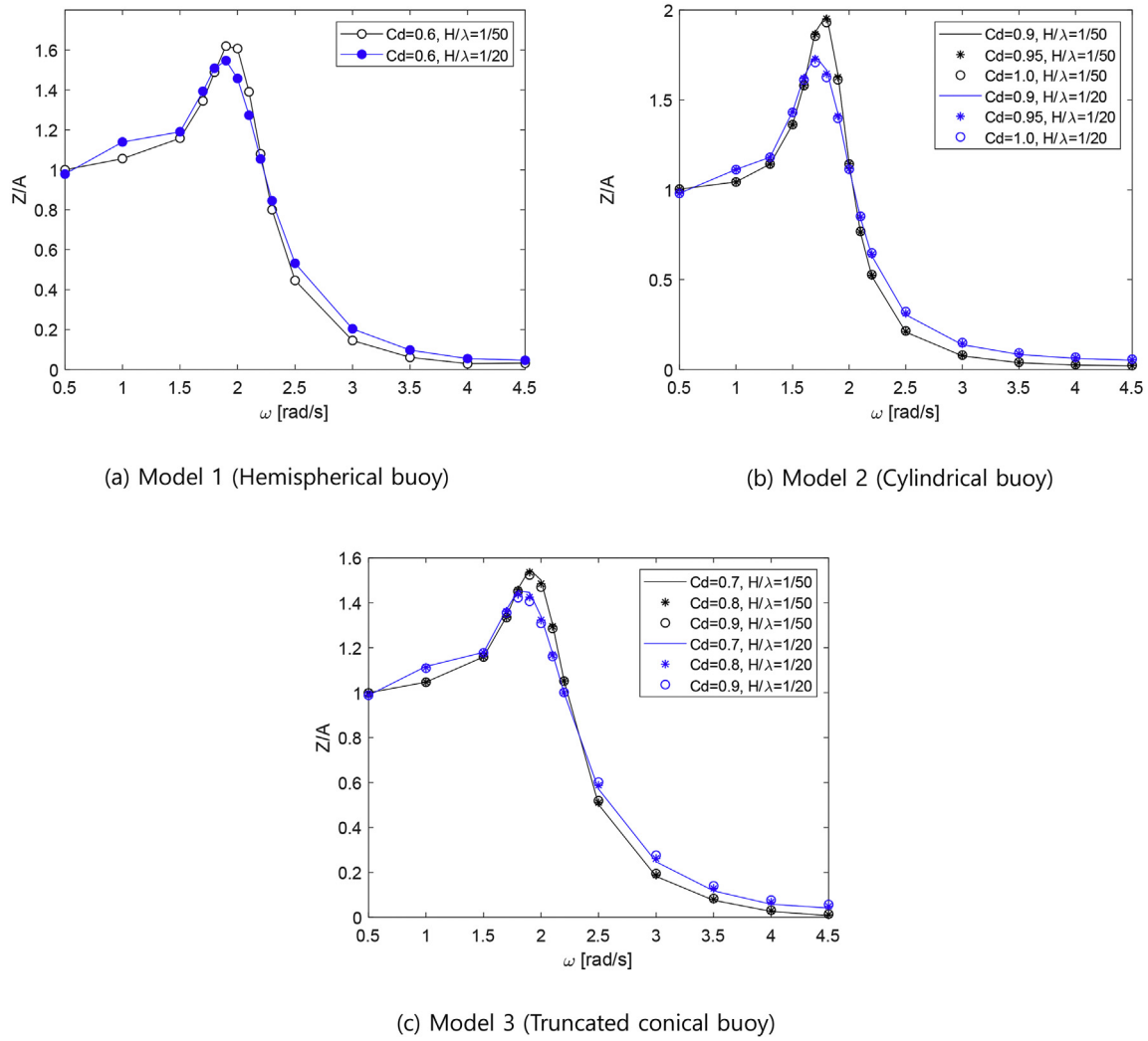

Fig. 7. Comparison of the heave RAOs including the drag forces (a: Hemispherical buoy, b: Circular cylindrical buoy, c: Truncated conical buoy).

nodes was 1200, 1770, and 1576, respectively. The Runge-Kutta 4th-order time integration method was adopted for time marching, and its time integration step was set to T/200.

Fig. 3 presents the heave RAOs of three different types of buoys for WEC. In the figure, Z means the amplitude of the heave motion displacement. All bodies had the same mass and restoring coefficients. On the other hand, owing to differences in the hydrodynamic coefficients, the cylindrical buoy with a relatively small draft has a heave natural frequency of approximately 1.8 rad/s, and the hemispherical and the conical bodies have a heave natural frequency of 2.0 rad/s. For the cylindrical buoy, the maximum heave response was approximately 2.8 times the incident wave amplitude.

Fig. 4 shows the heave RAOs of a hemispherical buoy from different methods of the Froude-Krylov force. Two different methods were adopted to evaluate the Froude-Krylov force: conventional frequency-domain linear analysis and a method based on the Maclaurin expansion, as shown in chapter 2.2. Convergence tests were performed to investigate how many terms of the theoretical solutions in the Maclaurin expansion are needed to calculate the accurate Froude-Krylov force. The effects of buoy displacement and wave elevation around the buoy were not considered in this test. In Fig. 4, the heave RAO applying the Froude-Krylov force from the Maclaurin expansion to the 4th-term was similar to the linear analysis results. In Fig. 5, convergence tests were also performed for the number of applied terms in the Maclaurin expansion for Model 2 (cylindrical buoy) and Model 3 (truncated cone buoy). To obtain accurate heave RAOs, models 2 and 3 were applied up to the 4th- and 6th-terms of the theoretical solution in the Maclaurin expansion.

Fig. 6 compares the nonlinear Froude-Krylov forces calculated by the theoretical solutions based on a Maclaurin expansion and the remeshing scheme according to the buoy displacement. The change in the incident wave potential in the z-direction above the mean water level was expressed by vertical stretching. For simplicity, it was assumed that the incident wavelength was long enough to ignore the diffraction effect, and the variation of wave elevation was the same as the heave response of the buoy. To apply the remeshing technique, the numerical model used in Fig. 2 for frequency-domain analysis was used. The linear Froude-Krylov force means the force calculated at the mean body posion without taking into account the instantaneous wetted body surface. The results of the theoretical solution agreed well with those of the remeshing scheme. On the other hand, the linear Froude-Krylov force had a constant value regardless of the buoy displacement. Through Fig. 6, as the buoy displacement increases, the

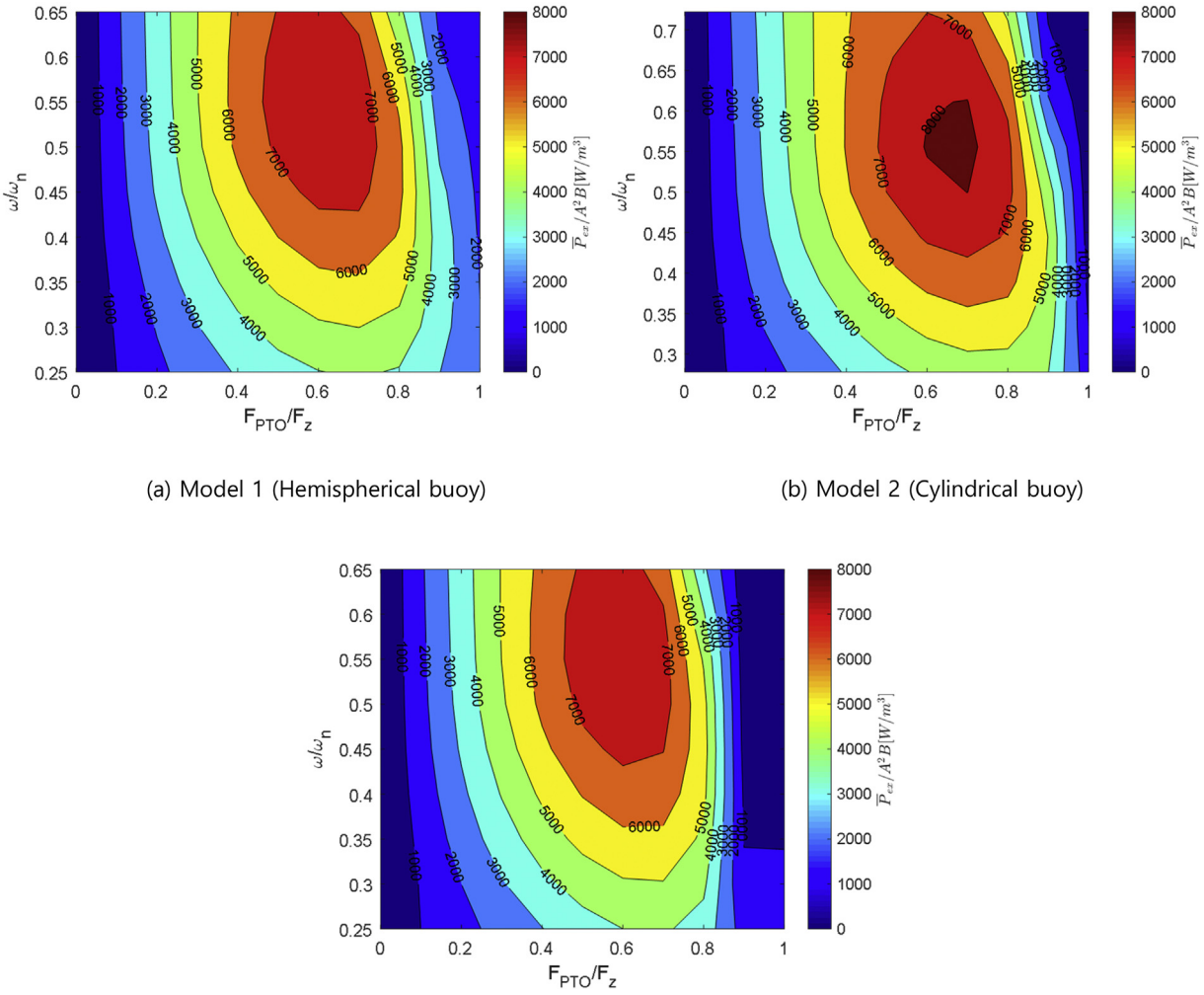

(a) Model 1 (Hemispherical buoy)

(b) Model 2 (Cylindrical buoy)

(c) Model 3 (Truncated conical buoy)

Fig. 8. Time-averaged extraction power on various PTO conditions (ω = 0.8 rad/s, H/λ = 1/50, Model 1(Hemispheric buoy)).

magnitude of the Froude-Krylov force increased approximately seven times more than the linear FK force.

Fig. 7 presents the heave RAOs of the buoy under two different wave steepness conditions with various drag coefficients. The results were calculated through the theoretical solutions with a given optimal series of a Maclaurin expansion. Even when the drag coefficients were applied, the sensitivity to the drag coefficient was quite small because the vertical motion of the body did not change significantly. In this study, the drag coefficient was 0.6, 0.95, and 0.8 for the hemispherical buoy, cylindrical buoy, and truncated conical buoy, respectively. The vertical motion decreased in the resonance period when the wave steepness was large (H/λ=1/20), but the motion increased slightly in the other wave periods. To estimate the energy extraction of WEC, the hydraulic PTO system was modeled numerically and applied. The optimal hydraulic PTO condition was determined from the case of a small amplitude wave ($H/\ \lambda$=1/50) for each numerical model. The hydraulic PTO condition can be expressed by the difference between the High Pressure (HP) and Low Pressure (LP) from the hydraulic cylinder and the flow rate. Fig. 8 presents the time-averaged extraction power under various PTO forces applied to three types of buoys for WEC. Various PTO damping values were applied to obtain the optimal PTO force condition in the wave wave region of $0.25 \ll \omega/\omega_n \ll 0.75$. The time-averaged generated power ($\overline{P}_{ex}$) was divided by the square of incident wave amplitude (A) and the buoy diameter (B) as $\overline{P}_{ex}/A^2B$ to estimate and compare the value according to the change in the incident wave period. The maximum time-averaged extraction energy occurred when the PTO force was 70% of the vertical excitation force of the buoy ($F_z = F_{FK} + F_D$). In this way, the PTO conditions for maximum energy extraction under various wave conditions were calculated for each numerical model of the buoy.

Based on the previously estimated conditions of the hydraulic PTO system as Fig. 8, the results of the weakly nonlinear time-domain analysis of a hemispherical buoy for a WEC were compared with the results of linear time-domain analysis (Fig. 9) at specific wave and PTO condition (ω/ω_n=0.4, F_{PTO}/F_z=0.7). A latching duration of 2.356 s, which is the optimal latching time at the corresponding frequency, was applied. The results of linear analysis and nonlinear analysis agreed well when the incident wave height was low at 0.25 m (H/λ= 1/240). This is because the incident wave belongs to the linear wave region. Therefore, the nonlinearity is small. When the wave amplitude increased, however, the relative heave response (Fig. 9 (a)) and the time-averaged extraction power compared to wave amplitude (Fig. 9 (b)) decreased. The static force

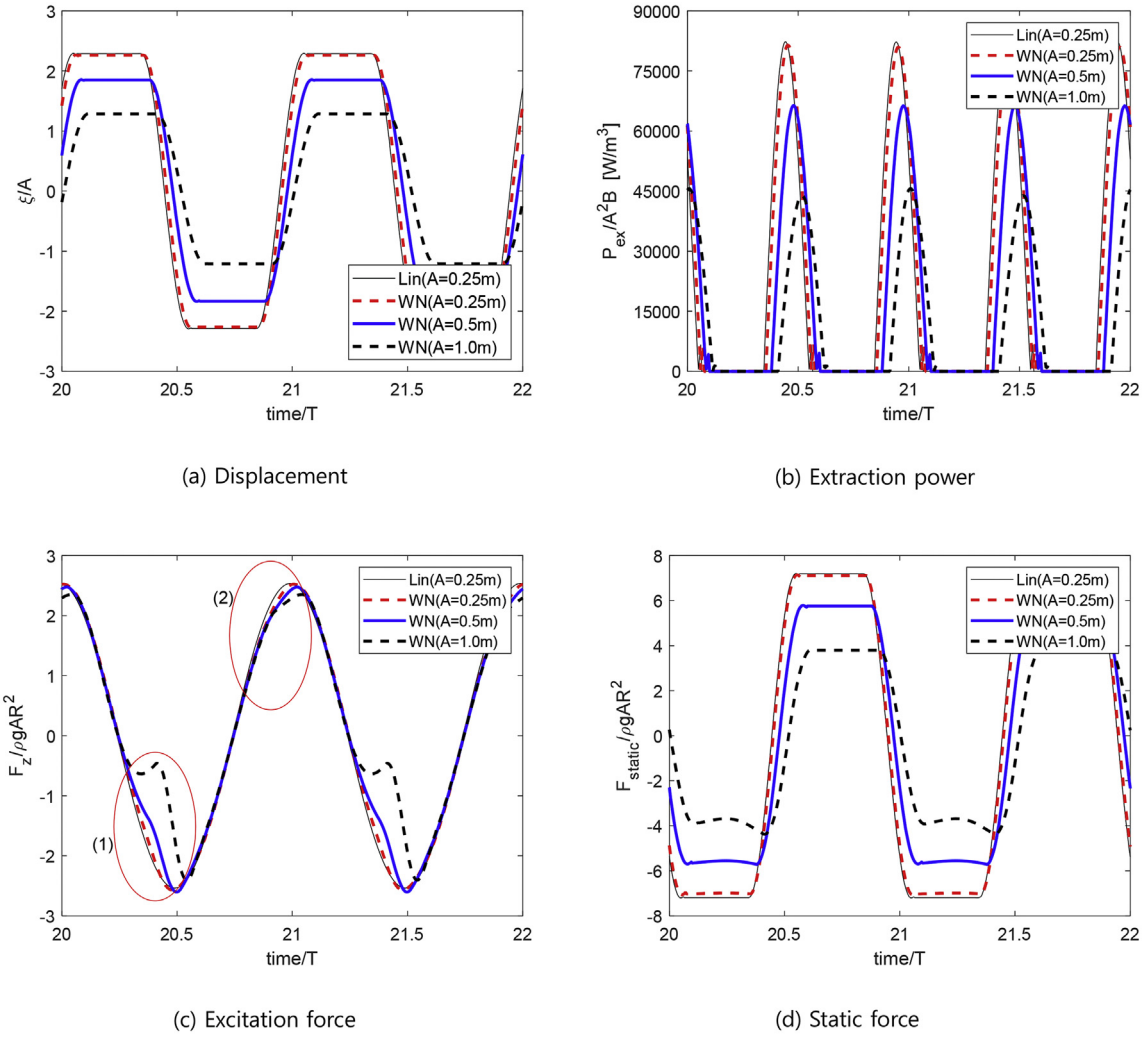

Fig. 9. Time-series of hemispherical buoy displacements, extraction powers, excitation forces and static forces ($\omega/\omega_n = 0.4$, $F_{PTO}/F_z = 0.7$, Lin: Linear analysis, WN: Weakly nonlinear analysis).

(Fig. 9 (d)) also decreased with increasing wave amplitude. Fig. 9 (c) shows the time series of the wave excitation forces, the sum of the Froude-Krylov force, and diffraction force under various wave amplitude conditions. Because the diffraction force does not differ between linear analysis and weakly nonlinear analysis, the difference in excitation force was due to the nonlinear Froude-Krylov force. As the wave amplitude increased, the nonlinear effect of the excitation force increased, as shown in Fig. 9(c). The latching control strategy enables the extraction of large amounts of energy with the effect of rapidly moving the body upward or downward. This technique can constrain the body motion during the latching duration, making a 90° difference in phase angle between excitation force and buoy motion. This can be confirmed by comparing the time when the buoy displacement is zero, and when the external force is zero. In Fig. 9 (c), indication (1) is when the buoy moves downward, and (2) is when the buoy moves upward. When the difference was 90°, the excitation force acting on the body was maximized along the direction of movement of the buoy after releasing the buoy motion according to the latching control strategy. As the incident wave amplitudes increased to 0.25 m, 0.5 m, and 1.0 m, the magnitude of the buoy motion decreased by 1%, 18.6%, and 32.3%, respectively, compared to the linear analysis results. The external force was also reduced at a similar rate.

Fig. 10 compares the heave RAOs and time-averaged extraction powers of three different WEC buoy models under a range of incident wave amplitudes. The analysis was performed only in the longwave condition, where the latching control strategy was known to be effective. For a clear comparison, the heave RAOs and time average extraction powers were compared when no latching control strategy was applied. The time-averaged extraction power was nondimensionalized by the incident wave flux, which is the same as the capture width. As shown in Fig. 9, as the amplitude of the incident wave increased, the displacement of the buoy decreased due to the influence of the nonlinear Froude-Krylov force, and the dimensionless time-averaged extraction power decreased. As the incident wave amplitude was increased from 0.25 m to 1.0 m, the extraction power ($\overline{P}/A^2B$) decreased from 50% to 20%. Based on these results, linear analysis using latching control techniques provides overestimated results. In addition, when the incident wave frequency was 0.4–0.5 times the natural frequency of the buoy, the heave RAO and time-averaged extraction power were maximized due to the latching control technique. Therefore, latching control is very effective when the wave height is small, and the incident wave frequency is 0.4–0.5 times the heave natural frequency of the buoy. Table 2 lists the maximum time-averaged extraction power for the three models under each calculation

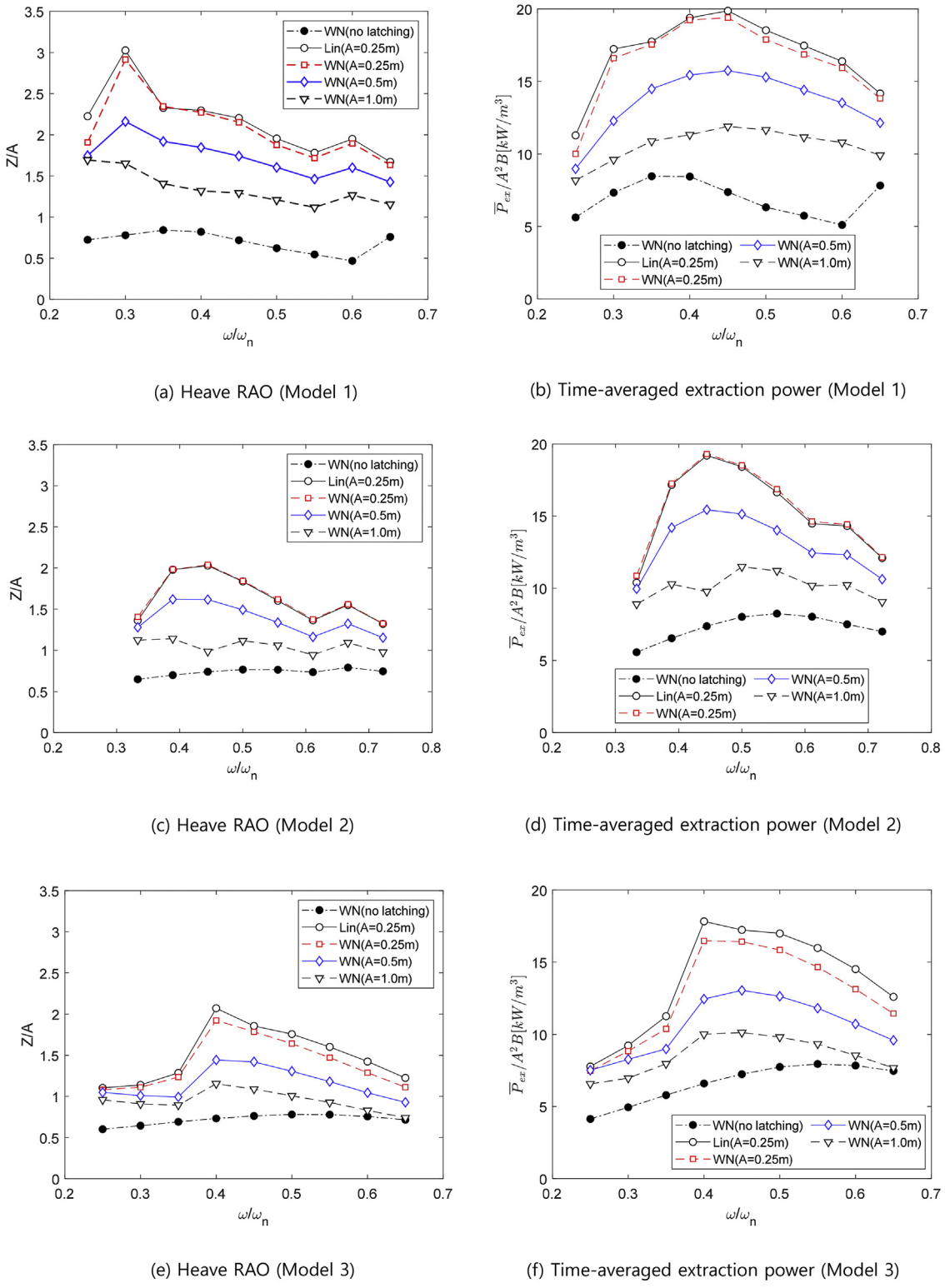

(a) Heave RAO (Model 1)

(b) Time-averaged extraction power (Model 1)

(c) Heave RAO (Model 2)

(d) Time-averaged extraction power (Model 2)

(e) Heave RAO (Model 3)

(f) Time-averaged extraction power (Model 3)

Fig. 10. Comparison of the heave RAOs and the time-averaged extraction powers for three different buoy models.

condition. When the wave amplitude was small (A = 0.25 m), the effect of latching control was amplified more than twice the maximum extraction power compared to the case without latching control. When the wave amplitude was large (A = 1.0 m), however, it was amplified by approximately 40%. When applying latching control, the cylindrical buoy and the spherical buoy have a slightly better power take-off performance than the truncated conical buoy.

Further analysis of a hemispherical buoy under irregular wave conditions was performed. In the case of irregular wave analysis, the same drag coefficient as the previous regular wave analysis was applied. The time interval was fixed to 0.01 s, and the analysis duration was fixed to the sea state duration of 3 h. Fig. 11 shows the

Table 2
Maximum time-averaged extraction power.

	Model1 [W/m^3]	Model2 [W/m^3]	Model3 [W/m^3]
WN(A = 0.25 m) (No latching control)	8469 (2626 W)	8236 (2573 W)	7945 (2483 W)
Lin(A = 0.25 m)	19,866 (6208 W)	19,192 (5997 W)	17,823 (5570 W)
WN(A = 0.25 m)	19,398 (6062 W)	19,296 (6030 W)	16,473 (5148 W)
WN(A = 0.50 m)	15,749 (19,686 W)	15,437 (19,296 W)	13,045 (16,306 W)
WN(A = 1.00 m)	11,900 (59,500 W)	11,487 (57,435 W)	10,123 (50,615 W)

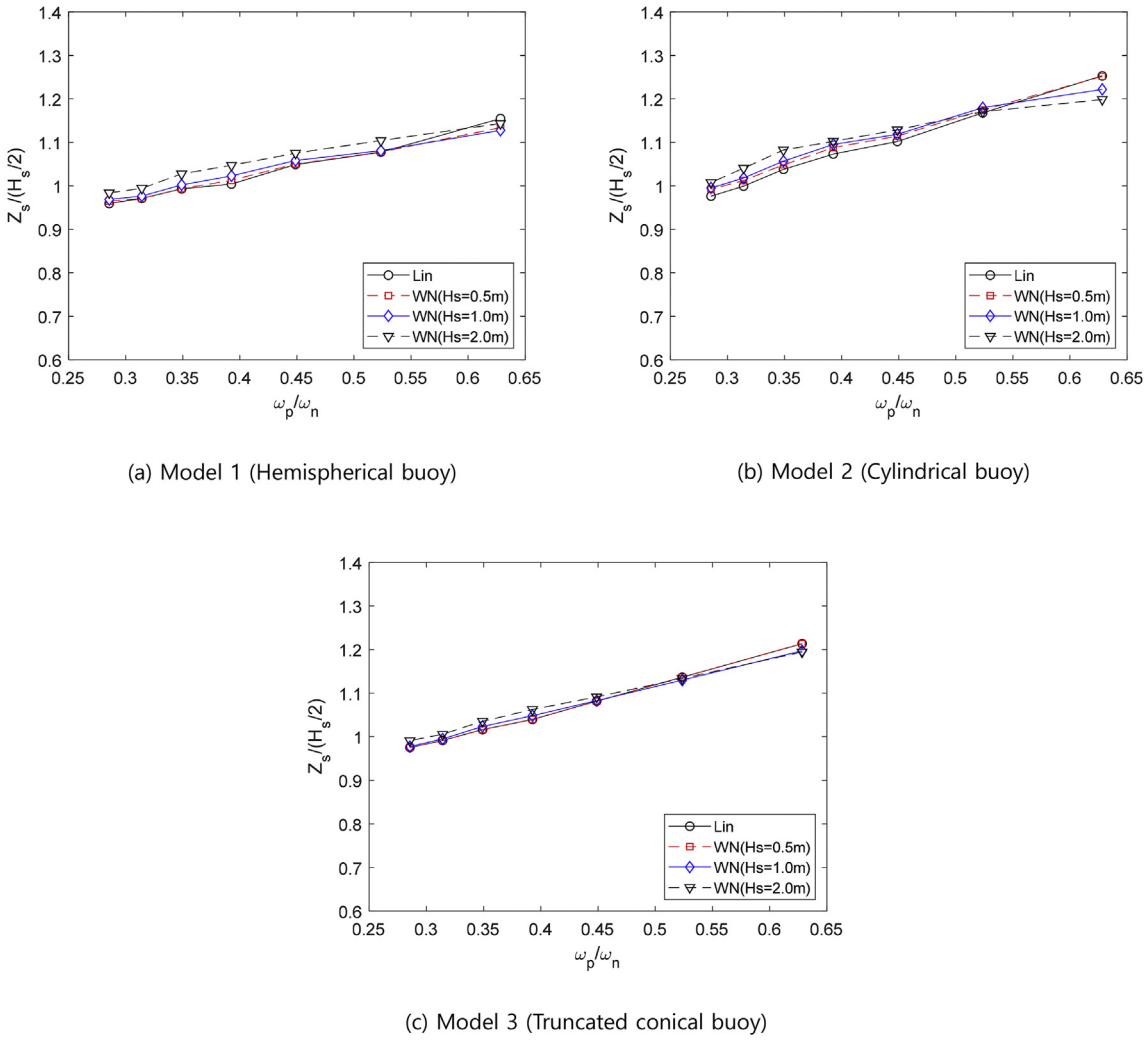

(a) Model 1 (Hemispherical buoy)

(b) Model 2 (Cylindrical buoy)

(c) Model 3 (Truncated conical buoy)

Fig. 11. Comparison of the significant buoy displacement on various significant wave heights.

significant displacements of each numerical model for various significant wave heights in the absence of a PTO force and the latching control strategy. The zero-crossing method was applied to calculate the significant buoy displacement. In the case of irregular wave analysis, since a random phase angle should be applied to each frequency component, the numerical analysis of a single wave condition (H_s and T_p) was repeated 10 times, and the average value was used. When the latching control strategy and PTO force were not applied, the change in the significant buoy displacement was not large. The overall amplitude tended to decrease with increasing wavelength (frequency decreases) and had a value similar to the significant wave height. This is because as the wavelength increases, the heave amplitude of the buoy becomes equal to the incident wave amplitude. In the comparison in Fig. 11, the significant displacements of the buoys in all numerical models are slightly larger than those of the linear analysis in the WN analysis because the amplitudes of the Froude-Krylov forces by larger displacements are increased as shown in Fig. 6. However, the differences are small.

Fig. 12 shows the time histories of the heave displacement, instantaneous extraction power, static force, and excitation force of a hemispherical buoy type WEC under various significant wave heights with optimal latching control. The PTO force for the maximum time-averaged power was estimated by trial and error ($F_{PTO}/F_z = 0.3$). The latching duration, the only variable in the latching control strategy, was set as Eq. (31). For this analysis, the same random phase angle was applied for each incident wave

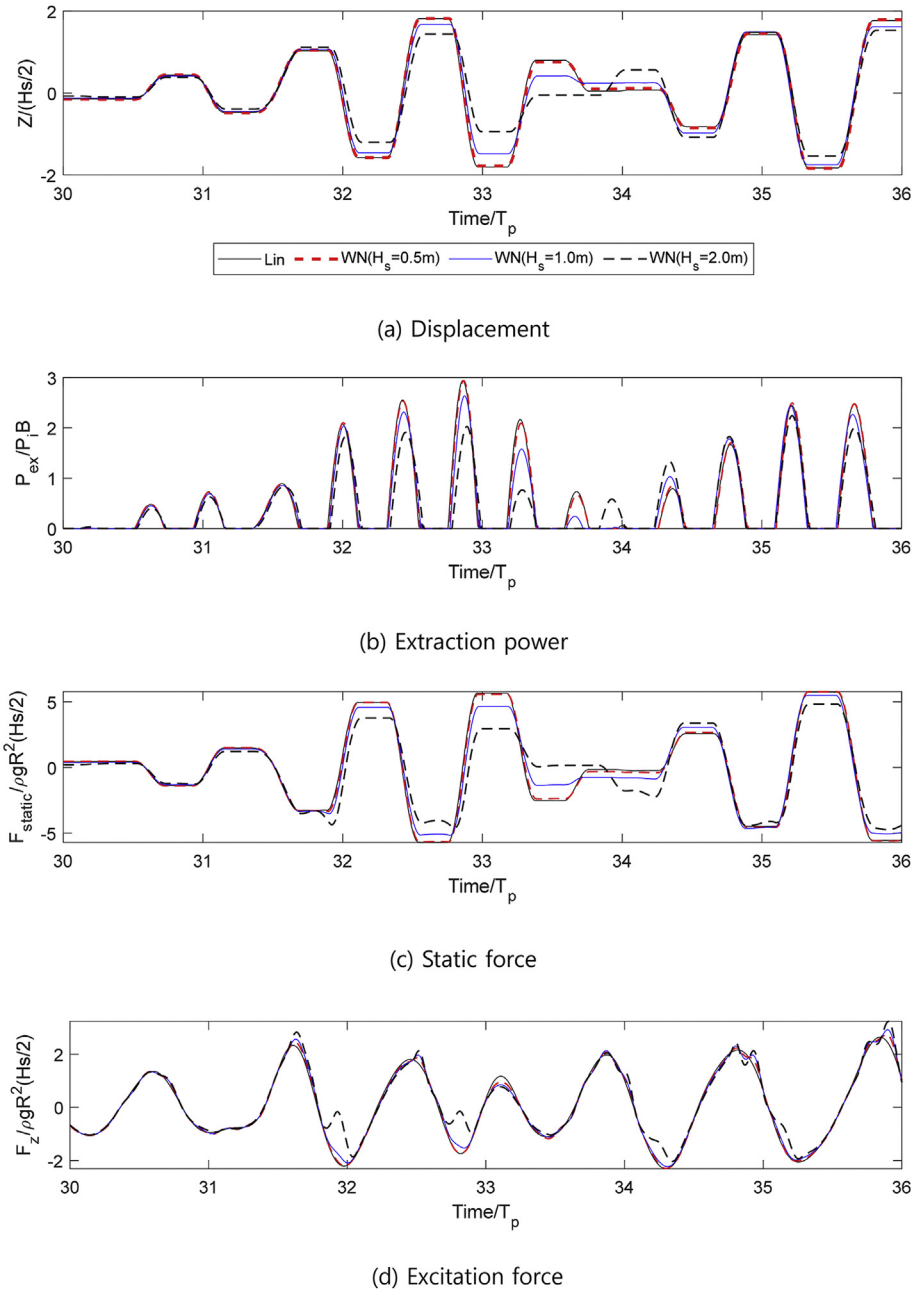

Fig. 12. Time histories of the buoy displacement, instantaneous extraction power, static force, and excitation force on various significant wave heights ($F_{PTO}/F_z = 0.3$, $\omega_P/\omega_0 = 0.45$, $T_L = 1.43$ s, Model 1).

frequency component. When the amplitude of the buoy displacement was small (the time range of 30 $\ll Time/T_p \ll$31.5), all the calculated values similar regardless of the amplitude of the incident wave. On the other hand, the results of nonlinear analysis varied as the displacement of the buoy increased. When the significant wave height was high, the displacement of the buoy changed rapidly by latching control, and the nonlinear static force and excitation force also changed nonlinearly.

Fig. 13 shows the time-averaged generated power for each numerical model as function of various PTO forces and wave peak frequencies of irregular waves. For this, weakly nonlinear analysis was carried out in irregular waves (Hs = 0.5 m) to obtain the optimal PTO force ratio (the ratio of PTO force to excitation force at each peak frequency, F_{PTO}/F_z). The optimal ratio (F_{PTO}/F_z) was 0.3–0.5 for all numerical models unlike the optimal ratio in regular waves (F_{PTO}/F_z = 0.5–0.7). Based on the results of Figs. 13 and 14 shows the significant displacement and the time-averaged extraction power under various peak frequencies and significant wave heights in irregular waves using a latching control strategy. The zero-crossing method was used to calculate the significant displacement and time-averaged extraction power. The optimal PTO conditions and the latching control for the maximum energy extraction were applied. This numerical analysis was performed in the longwave region, where the latching control technique was effective. The buoy displacement increased with increasing wavelength, but the displacement decreased with increasing significant wave height. When the ratio of the peak frequency to body resonant frequency (ω_p/ω_n) was increased from 0.4 to 0.45, the

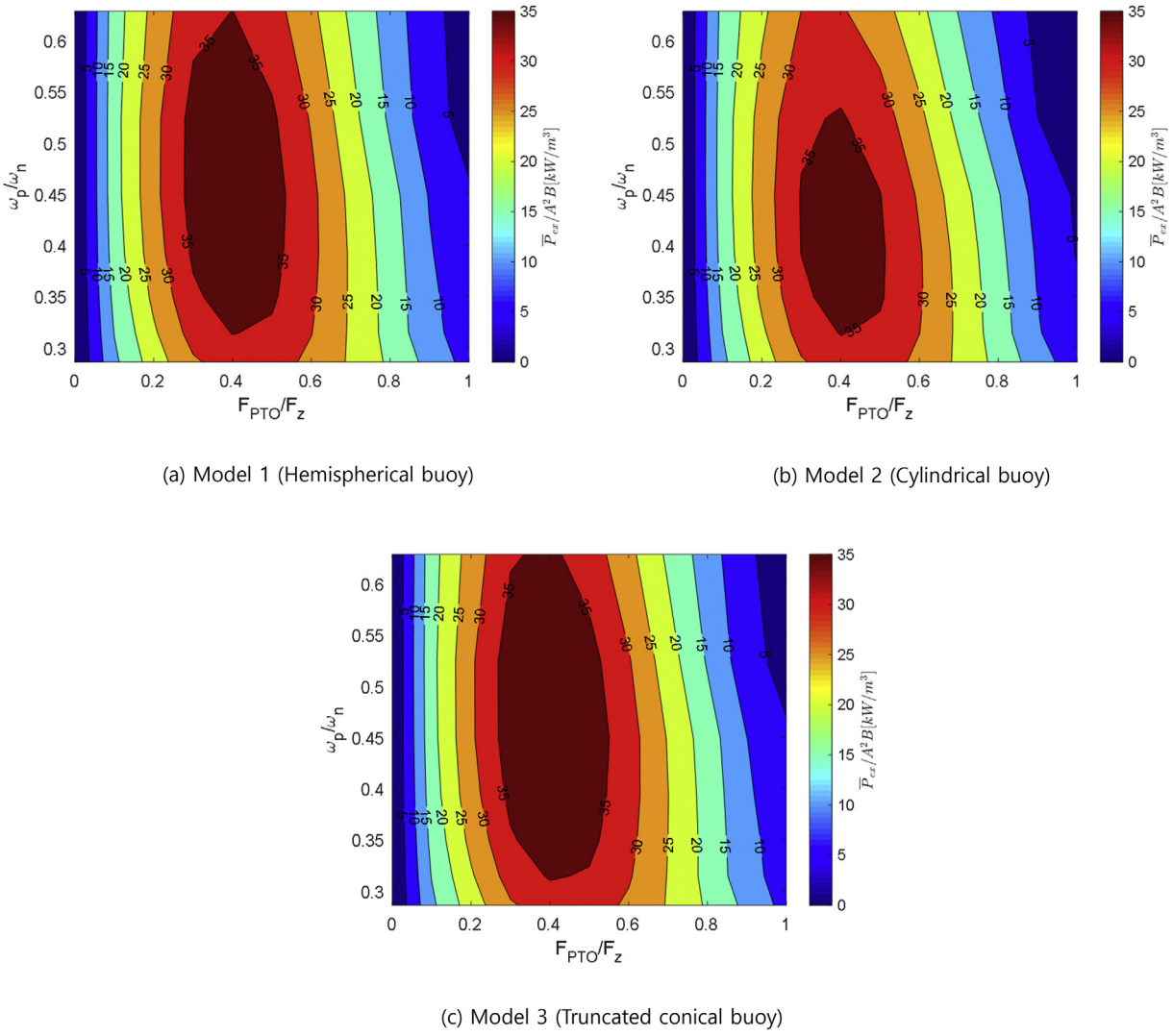

(a) Model 1 (Hemispherical buoy)

(b) Model 2 (Cylindrical buoy)

(c) Model 3 (Truncated conical buoy)

Fig. 13. Comparison of the time-averaged generated power on various PTO forces and wave peak frequencies (Weakly nonlinear analysis, Hs = 0.5 m).

maximum time-averaged extraction power occurred. Therefore, when designing the heaving hemispherical buoy type WEC to which the latching control was applied, it was effective to design the incident wave frequency at approximately 0.4–0.45 times the heave natural frequency of buoy. In addition, when the significant wave height was small (H_s= 0.5 m), the extraction power increased by 25–50% due to latching control. In contrast, when the significant wave height was large (H_s= 2.0 m), the latching control effect was increased by only 10–15%. As a result of estimating the influence of the buoy shape through Fig. 14(b)~(d), the trend of the time-averaged generated power was similar regardless of the shape of the buoy. However, the maximum generated power from the truncated conical buoy type WEC was smaller than the others. The cylindrical buoy WEC with high wave amplitude (H_s = 2.0 m) and latching control strategy produced less power than the case without latching control. Through this, nonlinear analysis is required to estimate the power take-off performance of the wave energy converter accurately under high wave conditions.

4. Conclusion

In this study, the nonlinear Froude-Krylov forces for three buoy forms (hemispherical, cylindrical, and truncated conical) for a heaving buoy type WEC were derived theoretically using the Maclaurin expansion method. The theoretical solutions of the nonlinear Froude-Krylov forces were applied to the WEC system using a latching control strategy. The coupled analysis between the buoy and the PTO system was carried out using a latching control strategy. To confirm the accuracy of the theoretical solutions, the heave RAOs of the buoy were compared with the results of linear analysis and the remeshing numerical scheme. The drag coefficients were also applied to each buoy to consider the viscous effect. Based on this, the hydrodynamic performance and extraction power under various wave conditions were evaluated for three types of heaving buoy WECs to which the latching control strategy had been applied, and the following conclusions were drawn.

1. An incident wave period of 0.4–0.45 times the natural period of the buoy was the optimal condition to amplify the extraction power of the WEC buoy through latching control. Under irregular wave conditions, the peak period of the incident wave was optimal between 0.4 and 0.45 of the natural period of the buoy.

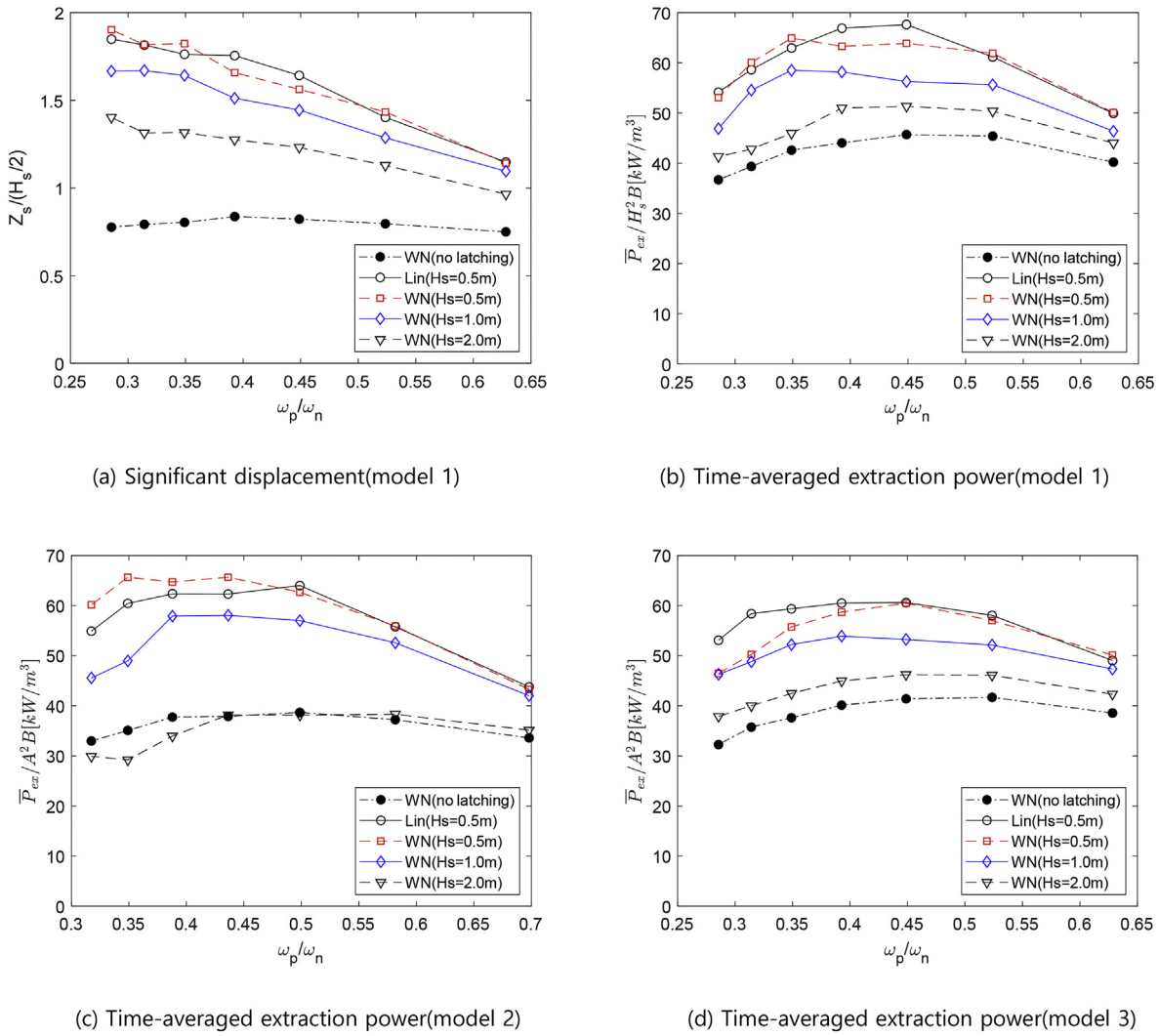

(a) Significant displacement(model 1)

(b) Time-averaged extraction power(model 1)

(c) Time-averaged extraction power(model 2)

(d) Time-averaged extraction power(model 3)

Fig. 14. Comparison of significant displacement of buoy and time-averaged extraction power on various irregular wave conditions (a, b: hemispherical buoy (Model 1), c: cylindrical buoy (Model 2), d: truncated conical buoy (Model 3)).

2. Among the three types of WEC heaving buoys under latching control, the hemispherical buoy showed the maximum energy extraction performance.
3. When the significant wave height was small (H_s= 0.5 m), the extraction power increased by 25–50% due to latching control, but the latching control effect was increased by only 10–15% when the significant wave height was large (H_s= 2.0 m). Through this, nonlinear analysis is required to estimate the power take-off performance of the wave energy converter accurately under high wave conditions.

Declaration of competing interest

The authors declare that they have no known competing financial interests or personal relationships that could have appeared to influence the work reported in this paper.

Acknowledgments

This research was supported by the MOTIE (Ministry of Trade, Industry, and Energy) in Korea, under the Fostering Global Talents for Innovative Growth Program (P0008750) supervised by the Korea Institute for Advancement of Technology (KIAT). This research was also supported by Basic Science Research Program through the National Research Foundation of Korea (NRF-2018R1D1A1B07040677 and 2018R1A6A3A01013558).

References

Babarit, A., Mouslim, H., Clement, A., Laporte-Weywada, P., 2009. On the numerical modelling of the non linear behavior of a wave energy converter. In: Proceedings of the ASME 2009 28th International Conference on Ocean. Offshore and Arctic Engineering, Honolulu, Hawaii, USA.

Babarit, A., Hals, J., Muliawan, M.J., Kurniawan, A., Moan, T., Krokstad, J., 2012. Numerical benchmarking study of a selection of wave energy converters. Renew. Energy 41, 44–63.

Cho, I.H., 2015. Latching control technology for improvement of extracted power from wave energy converter. Journal of the Korean Society for marine Environment and Energy 18 (4), 282–290.

Falcao, A.F.O., 2008. Phase Control through Load control of oscillating-body wave energy converters with hydraulic PTO system. Ocean. Eng. 35 (3–4), 358–366.

Folley, M., Henryand, A., Whittaker, T., 2015. Contrasting the hydrodynamics of heaving and surging wave energy converter. In: Proceedings of the 11th European Wave and Tidal Energy Conference, Nantes, France..

Giorgi, G., Penalbe, M., Ringwood, J., 2016. Nonlinear hydrodynamic models for heaving buoy wave energy converters. In: Proceedings of Asian Wave and Tidal Energy Conference. AWTEC), Singpore, pp. 144–153.

Giorgi, G., Ringwood, J.V., 2017. Computationally efficient nonlinear Froude-Krylov force calculations for heaving axisymmetric wave energy point absorbers.

Journal of Ocean Engineering and Marine Energy 3 (1), 21–33.
Giorgi, G., Ringwood, J.V., 2018. Analytical representation of nonlinear Froude-Krylov forces for 3-DoF point absorber wave energy devices. Ocean. Eng. 164, 749–759.
Gudmestad, O.T., Meo, G., 1996. Hydrodynamic coefficients for calculation of hydrodynamic loads on offshore truss structures. Mar. Struct. 9, 745–758.
Guo, B., Patton, R.J., Jin, S., Gilbert, J., Parsons, D., 2018. Nonlinear modelling and verification of a heaving point Absorber for wave energy conversion. IEEE Transactions of Sustainable Energy 9 (1), 453–461.
Hal, J., Falnes, J., Moan, T., 2011. A comparison of selected strategies for adaptive control of wave energy converters. J. Offshore Mech. Arctic Eng. 133 (3), 031101-1-12.
Jang, H.K., Kim, M.H., 2020. Effects of nonlinear FK and hydrostatic restoring forces on arctic spar motions in waves. International Journal of Naval Architecture and Ocean Engineering 12, 297–313.
Kalofotias, F., 2016. Study for the Hull Shape of a Wave Energy Converter-point Absorber; Design Optimization and Modeling Improvement. Master's thesis, University of Twente.
Kim, J., Cho, I.H., Kim, M.H., 2019a. On numerical calculation and experiment of a heaving-buoy wave energy converter with a latching control, Ocean Systems Engineering. Int. J. 9 (1), 1–19.
Kim, S.J., Koo, W., Jo, C.H., 2019b. Assessment of latching control for the hemispheric heaving buoy type point absorber with and without nonlinear Froude-Krylov force acting on the buoy. In: Proceedings of the ASME 2019 38th International Conference on Ocean. Offshore and Arctic Engineering, Glasgow, Scotland, UK.
Kim, S.J., Koo, W., Shin, M.J., 2019c. Numerical and experimental study on hemispheric point-absorber-type wave energy converter with a hydraulic power take-off system. Renew. Energy 135, 1260–1269.
Lok, K.S., Stallard, T.J., Stansby, P.K., Jenkins, N., 2014. Optimisation of a clutch-rectified power take off system for a heaving wave energy device in irregular waves with experimental comparison. International Journal of Marine Energy 8, 1–16.
Merigaud, A., Gilloteaux, J.C., Ringwood, J.V., 2012. A nonlinear extension for linear boundary element methods in wave energy device modelling. In: Proceedings of the ASME 2012 31st International Conference on Ocean. Offshore and Arctic Engineering, Rio de Janeiro, Brazil.
Nazari, M., Ghassemi, H., Ghiasi, M., Sayehbani, M., 2013. Design of the point absorber wave energy converter for Assaluyeh port. Iran. J. Energy Environ. 4 (2), 130–135.
Sarpkaya, T., 1986. Force on a circular cylinder in viscous oscillatory flow at low Keulegan-Carpenter numbers. J. Fluid Mech. 165, 61–71.
Sheng, W., Alcorn, R., Lewis, A., 2015. On improving wave energy conversion, part II: development of latching control technologies. Renew. Energy 75, 935–944.
WAMIT User Manual V. 7.3, 2019. WAMIT, Inc.
Zurkinden, A.S., Ferri, F., Beatty, S., Kofoed, J.P., Kramer, M.M., 2014. Nonlinear numerical modeling and experimental testing of a point absorber wave enregy converter. Ocean. Eng. 78, 11–21.